Inter- and intrachannel exchange interference in photoinduced Auger decay: The Kr $M_{4,5}$–N_1N_{23} and Xe $N_{4,5}$–O_1O_{23} cases

M Žitnik,* K. Bučar, and A. Mihelič
Jožef Stefan Institute, P.O. Box 3000, SI-1001 Ljubljana, Slovenia and Faculty of Mathematics and Physics, University of Ljubljana, Jadranska 19, SI-1000 Ljubljana, Slovenia

P. Lablanquie, F. Penent, J. Paladoux, and L. Andrić
UPMC, Université Paris 06, LCPMR, 11 rue Pierre et Marie Curie, 75231 Paris Cedex 05, France and CNRS, LCPMR (UMR 7614), 11 rue Pierre et Marie Curie, 75231 Paris Cedex 05, France

P. Bolognesi and L. Avaldi
CNR-IMIP, Area della Ricerca di Roma 1, CP10, 00015 Monterotondo Scalo, Italy
(Received 26 July 2012; revised manuscript received 30 December 2012; published 31 January 2013)

We study interference effects that appear in the cross section due to detection of two indistinguishable electrons in a photoelectron–Auger-electron *pair* (intrachannel exchange interference), or due to detection of two indistinguishable photoelectron-Auger electron *pairs* that share the final state but are emitted via two different intermediate states (interchannel exchange interference). For photoinduced Kr $M_{4,5}$–N_1N_{23} (Xe $N_{4,5}$–O_1O_{23}) Auger decay, the intrachannel exchange interference is "switched on" at 131.3 eV (87.0 eV) and 133.8 eV (91.0 eV) photon impact energy for the M_5 (N_5) and M_4 (N_4) holes, respectively. The interchannel exchange interference is expected to appear at 132.6 eV (89.0 eV) when the photoelectron ejected from the M_4 (N_4) subshell is emitted with the same energy as the Auger electron emitted in the decay of the M_5 (N_5) hole, and vice versa, the energy of the photoelectron ejected from the M_5 (N_5) subshell equals the energy of the Auger electron emitted in the decay of the M_4 (N_5) hole. We use the approach of Vegh and Macek [Phys. Rev. A **50**, 4031 (1994)], and Vegh [Phys. Rev. A **50**, 4036 (1994)] to model these phenomena in a unified manner and examine their effects in an angle-resolved and angle-integrated coincidence spectra considering also the postcollision interaction (PCI). The previous and the present angle-resolved experimental results, together with the data obtained by a magnetic bottle time-of-flight spectrometer, indicate that in this particular case the exchange interference effects in the angle-integrated cross sections are considerably weaker than in the angle-resolved (γ,2e) cross sections.

DOI: 10.1103/PhysRevA.87.013436 PACS number(s): 32.80.Aa, 32.80.Hd

I. INTRODUCTION

In quantum mechanics, an outcome of a measurement depends on magnitudes *and* relative phases of amplitudes pertaining to indistinguishable reaction paths. The so-called complete scattering experiments [1] are designed to measure *all* amplitudes for a given quantum process and enable an ultimate model testing. In atomic physics successful attempts of determination of partial amplitudes for photoelectron emission [2–6], photoinduced autoionization and Auger decay [7,8], photodouble ionization [9,10], and fluorescence from degenerate magnetic sublevels populated by electron impact [11,12] are reported. These experiments usually require an energy and angle-resolved coincidence detection of electron-electron or electron-photon pairs taking part in the reaction and may involve preparation of the target or projectile beam in specific polarization states. Another important class of phenomena originates in interference of reaction paths going through nondegenerate but still overlapping excited states. This is manifested, for example, by the quantum beats in time spectra [13], a modulation of the angular distribution induced by the spin-orbit multiplet splitting [14], or by distortion of photoinduced resonant Auger [15,16], fluorescence [17], and x-ray spectra [18]. Finally, the processes involving nonoverlapping excited states can be made to interfere if at least two indistinguishable particles are present in the common final state [19]. This represents a unique opportunity for the measurements of relative amplitudes of processes proceeding through "distant" excited states.

To illustrate the last situation, we assume that two inner-shell ionization thresholds 1 and 2 with corresponding excitation energies E_1 and E_2 are involved in photoionization of an atomic ground state g and that both intermediate ionic states ${i_1}^+$ and ${i_2}^+$ decay to the same final state of a doubly charged ion f^{2+} by an Auger electron emission:

$$\begin{array}{ll} & {i_1}^+(E_1)+e\rightarrow e_1(\epsilon_A)+e_1(\epsilon_B)+f^{2+}(E_F) \\ & \nearrow \qquad (1) \\ g(0)+\gamma(E_\gamma) & \\ & \searrow \qquad (2) \\ & {i_2}^+(E_2)+e\rightarrow e_2(\epsilon'_A)+e_2(\epsilon'_B)+f^{2+}(E_F). \end{array}$$

Two electrons with energies ϵ_A and ϵ_B or ϵ'_A and ϵ'_B are present in the final state. The interference may appear in two ways, depending on the choice of the photon impact energy E_γ. The intrachannel exchange interference occurs when the two electrons in the final state of the same process, (1) *or* (2), do

*matjaz.zitnik@ijs.si

not differ enough in energy ($\epsilon_A \approx \epsilon_B$ or $\epsilon'_A \approx \epsilon'_B$) to be distinguished on account of the time delay of Auger emission with respect to the photoionization [20]. Such interference effects have been detected in angle-resolved $(\gamma,2e)$ measurements of the autoionizing Ne^+ $(2s2p)^{-1}3p\ ^2S$ resonance [21,22] and in a photoinduced N_5–OO Auger decay in Xe leading to the $5p^{-2}\ ^1S$ [23,24], $(5s5p)^{-1}\ ^1P$, and $5s^{-2}\ ^1S$ final states [25]. The interchannel exchange interference implies the coherence of paths through nondegenerate states [26]. It occurs when the energy of the photoelectron in path (1) equals the Auger electron energy in path (2), and vice versa ($\epsilon_A \approx \epsilon'_B$ and $\epsilon_B \approx \epsilon'_A$). Van den Brink *et al.* were the first to focus on such a specific situation that occurs also in electron impact excitation of autoionizing resonances [19]. To explain the measured spectra for helium, they generalized the well-known Fano parametrization of the resonance profile by including an interchannel interference term that is "switched on" only when the electron impact energy is properly chosen. de Gouw *et al.* [27] applied the same parametrization for photoionization followed by Auger decay: a straightforward noncoincidence measurement was required to detect coherence of processes involving decay of the Ar^+ $2p_{3/2}^{-1}$ and $2s_{1/2}^{-1}$ states that are separated 75 eV in energy. A subtle change in photoelectron line shape was observed when the incoming photon energy was adjusted such that photoelectrons ejected from the $2s$ orbital overlapped in energy with L_3–$M_{23}M_{23}(^1D_2)$ Auger electrons. Such a measurement implicitly integrates over the whole solid angle of the unobserved electron (photoelectron ejected in the creation of the $2p_{3/2}$ hole or the L_1–$M_{23}M_{23}$ electron emitted in Coster-Kronig decay of the $2s$ hole). A similar study was reported for a Kr^+ $3d_{5/2,3/2}^{-1}$ pair of intermediate states decaying to the $Kr^{2+}(4s4p)^{-1}\ ^1P$ final state [28]. Finally, the interchannel exchange interference was observed to modify the angular distribution of electron pairs in the Kr M_5–$N_1N_{2,3}$ Auger decay into the ^1P final state [29]. Below we report a study of the interchannel exchange interference effect for the decay of the Xe^+ $4d_{5/2,3/2}^{-1}$ doublet to $Xe^{2+}(5s5p)^{-1}\ ^1P$ state using the energy and angular resolved $(\gamma,2e)$ measurement. We also repeated a part of the measurement by Selles *et al.* [25] to characterize the intrachannel exchange interference effect on Xe^+ $4d_{5/2}^{-1}$.

It is known that when the same partial wave is populated by both emitted electrons, the exchange interference effects partially "survive" the angular integration [27]. For a pair of spin-orbit split holes, both with even parity, this condition is met for odd parity final states. Below we investigate two such cases, the Kr $M_{4,5}$–$N_1N_{2,3}$ and Xe $N_{4,5}$–$O_1O_{2,3}$ ones, in spectra measured by the magnetic-bottle-type time-of-flight (MB-TOF) spectrometer [30]. MB-TOF has been recently demonstrated to allow an efficient collection of angle-integrated electron-electron multicoincidence data [31], and it is important to find out how this new instrumentation can further studies in the field. The selected approach is somewhere between the noncoincidence Auger spectroscopy detecting a single electron from the coincidence pair and an angle-resolved $(\gamma,2e)$ experiment. An advantage over the first is that the coincidence signal is not diluted by a partial decay rate into a selected final state. On the other hand, while the $(\gamma,2e)$ experiment may be set to access specific experimental configurations with pronounced interference effects, the coverage of an extended angular range is time consuming.

Another motivation for this work stems from the fact that the general approach with the cross-section formulas in the closed form was never applied to the experimental data obtained after the publication of Vegh (and Macek) papers [20,26] in 1994. The discussion in [25,29] deals with the phase difference between the direct and exchange amplitude that is indeed in the core of the interference effect. The probability for $(\gamma,2e)$ reaction is calculated directly from the absolute square of the amplitude, and scalar invariants of the corresponding cross section [32] are not discussed. Such an approach may be adequate for an angle-integrated cross section because a good localization of the interference effect in the energy space results in a single phase shift. However, a phase shift that "causes" the interference effect at a particular angular setting depends on the selection of the electron detection angles. A general (model independent) way to parametrize multidifferential cross sections has to deal with weights of scalar invariants. As demonstrated below, singly and doubly angle- or/and energy-integrated cross sections, as well as the corresponding interference effects may be easily assessed by such a set of parameters, calculated at critical photon energy. In addition, we show how the approach with the scalar invariants may be expanded to include the effect of postcollision interaction.

II. EXPERIMENT

The first part of the experiment was performed at PLEIADES undulator beamline at Soleil synchrotron, France [33]. A single bunch operation in the top-up mode of the storage ring provided stable pulses of light every 1184 ns. The coincidence data were obtained by MB-TOF apparatus described previously in Ref. [34]. Briefly, a combination of a localized and strongly inhomogeneous magnetic field and of a weak uniform magnetic field collects electrons from the ionization volume and guides them onto the MCP detector at the other end of the 2-m long tube. Multielectron coincidences are extracted from differences of electron arrival times (STOPS) with respect to the light pulse (START) measured by the multihit time-to-digital converter. Time-to-energy conversion is calibrated by measuring TOF spectra of Kr and Xe photoelectrons in coincidence with Auger electrons of known kinetic energies. We recorded coincidence events leading to the $Kr(4s4p)^{-1}$ and $Xe(5s5p)^{-1}\ ^1P$ final states in the 124–140 and 80–105-eV photon energy range, respectively, using linearly polarized light with 0.2 eV energy step. The spectrometer was operating with about $\Delta E/E = 1.4\%$ energy resolution, and the measured detection efficiency was of the order of 65%. The signal of the selected final state is presented in Fig. 1 by four coincidence peaks whose positions depend on the photon energy—they partially overlap at critical (interference) photon energies, as discussed below. Although in the angle-integrated case only two coincidence peaks are actually observed (with respect to the common START signal the STOP signal of the faster electron on the MCP detector is always before the STOP signal of the slower electron on

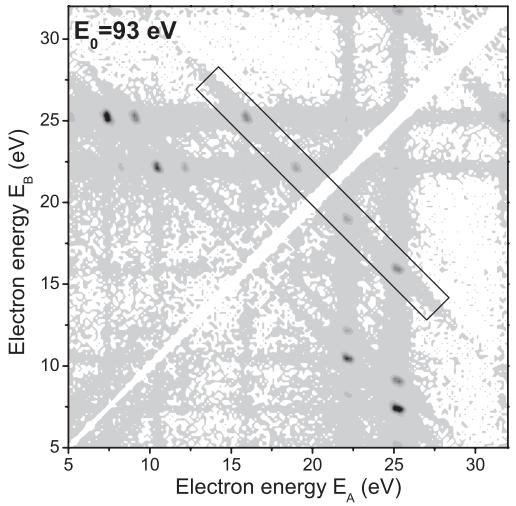

FIG. 1. An excerpt of an angle-integrated coincidence energy map acquired by MB-TOF in 10 min at 93 eV photon energy. A rectangular frame delimits coincidence events that belong to photoinduced Xe $N_{4,5}$–$O_1O_{2,3}$ Auger decay to the ^1P state. The maximum number of events in the pixel is about 1000. A white strip along the diagonal with no coincidence counts is due to the detector dead time that prevents detection of the coincidence event when both electrons have similar energies.

the same detector), the view is expanded to the full plane presentation. Apart from easier identification of the blind areas due to the MB-TOF dead-time effect (≈6 ns), such a presentation is clearly more suitable to describe $(\gamma,2e)$ measurements for a general case of two independent electron spectrometers each having its specific energy resolution and acceptance solid angle.

The second part of the experiment was performed at the Gasphase Photoemission undulator beamline at Elettra synchrotron, Italy [35], using a multicoincidence chamber with ten independent electron analyzers [36]. We measured $(\gamma,2e)$ angular distribution of the Xe^+ $4d_{5/2,3/2}^{-1}$ photoelectron and Auger electron leading to the Xe $(5s5p)^{-1}$ ^1P final state under and out of the interference conditions. The same apparatus has been used previously to investigate intrachannel exchange interference in the Kr case [29]. For the Xe measurement, the experimental energy resolution was 250 meV and the angular resolution was 8°. The results for one electron detected along the light polarization agree with the previous results concerning intrachannel interference of Xe [25], and new data are gathered about $(\gamma,2e)$ angular distribution under the interchannel exchange interference conditions.

III. THEORY

As the amplitude for the direct two-electron photoexcitation far away from threshold is relatively small, the cross section for production of the final state with energy E_F is given by the absolute square of the amplitude for the photoinduced Auger decay. This depends on energy and polarization state of light and in the most general case (involving two thresholds) has four contributions—a direct (T) and exchange (W) amplitude for each of the two paths:

$$
\begin{aligned}
T_1 &= \sum_{M_1} \frac{\langle \mathbf{k}_B\sigma_B J_F M_F|V|J_1M_1\rangle\langle J_1M_1\mathbf{k}_A\sigma_A|D|g,E_\gamma\lambda\rangle}{\epsilon_A - E_{\gamma 1} - i\Gamma_1/2},\\
W_1 &= \sum_{M_1} \frac{\langle \mathbf{k}_A\sigma_A J_F M_F|V|J_1M_1\rangle\langle J_1M_1\mathbf{k}_B\sigma_B|D|g,E_\gamma\lambda\rangle}{\epsilon_B - E_{\gamma 1} - i\Gamma_1/2},\\
T_2 &= \sum_{M_2} \frac{\langle \mathbf{k}_B\sigma_B J_F M_F|V|J_2M_2\rangle\langle J_2M_2\mathbf{k}_A\sigma_A|D|g,E_\gamma\lambda\rangle}{\epsilon_A - E_{\gamma 2} - i\Gamma_2/2},\\
W_2 &= \sum_{M_2} \frac{\langle \mathbf{k}_A\sigma_A J_F M_F|V|J_2M_2\rangle\langle J_2M_2\mathbf{k}_B\sigma_B|D|g,E_\gamma\lambda\rangle}{\epsilon_B - E_{\gamma 2} - i\Gamma_2/2}.
\end{aligned}
\tag{3}
$$

The intermediate singly ionized states $|J_1M_1\rangle$ and $|J_2M_2\rangle$, as well as the final doubly ionized state $|J_FM_F\rangle$ are denoted by the corresponding total angular momentum and its projection. The ejected electrons are characterized by the momenta $\mathbf{k}_A$, $\mathbf{k}_B$ and spin projections σ_A, σ_B. Energy differences E_i–E_j are abreviated by E_{ij}, while electron-electron interaction and electron-photon dipole interaction are denoted by $V = \sum_{i>j} 1/r_{ij}$ and $D = \mathbf{e}\cdot\sum_i \mathbf{r}_i$, respectively. Helicity of the incident light is described by λ.

Energy conservation requires the sum of electron energies $\epsilon_A+\epsilon_B$ to be close to the energy difference $E_{\gamma F}$, or practically equal to it when the natural linewidth of the final state is negligible. When the energies of the four electrons are substantially different, the corresponding triply differential cross section (TDCS) is proportional to the sum of absolute squares of the four amplitudes, summed over the (unresolved) final states:

$$
\frac{d^3\sigma}{d\epsilon_A d\Omega_A d\Omega_B} \propto \sum_{\sigma_A\sigma_B M_F} |T_1|^2 + |W_1|^2 + |T_2|^2 + |W_2|^2. \tag{4}
$$

Each of these terms corresponds to a peak in the coincidence energy plane (ϵ_A,ϵ_B) that is measured by sweeping independently the transmission energies of detectors A and B placed at angles Ω_A and Ω_B, respectively, with respect to some preferential direction. If the energy difference between the intermediate states is much larger than any of their natural linewidths Γ_1 and Γ_2, three special cases may be considered that are distinguished by the specific overlap of coincidence peaks. In the vicinity of the specific (critical) photon impact energies E_γ^c, the TDCS terms of Eq. (4) must be modified accordingly:

$$
\begin{aligned}
&(1)\ E_\gamma^c = 2E_1 - E_F \quad \rightarrow\ |T_1 - W_1|^2 + |T_2|^2 + |W_2|^2,\\
&(2)\ E_\gamma^c = 2E_2 - E_F \quad \rightarrow\ |T_1|^2 + |W_1|^2 + |T_2 - W_2|^2,\\
&(3)\ E_\gamma^c = E_1 + E_2 - E_F \rightarrow\ |T_1 - W_2|^2 + |T_2 - W_1|^2.
\end{aligned}
\tag{5}
$$

The first two cases are similar in nature. They occur when the coincidence event may be interpreted as an Auger electron click in detector A and a photoelectron click in detector B or vice versa. Such an intrachannel exchange interference is possible in a narrow range of E_γ when the two electrons along the same path (1 or 2) have their energies equal to within the uncertainty given by the natural width of the intermediate state. In case 3), the energies of electrons emitted along the same paths are different but there is an ambiguity of whether the coincidence event originates in path 1 or 2: one cannot

distinguish whether a coincidence event came from a click in detector A triggered by Auger electron from path 1 and a click in detector B triggered by the photoelectron from path 1, or from a click in detector A triggered by the photoelectron 2 and a click B triggered by the Auger electron 2. The interchannel exchange effect obviously requires the energy of Auger electron 1 to be equal to the energy of the photoelectron 2 (the energy of Auger electron 2 is then automatically equal to the energy of photoelectron 1).

When the two intermediate states partially overlap, i.e., when $|E_2 - E_1| \approx \Gamma_1, \Gamma_2$, the interference contribution of such quasidegenerate states must be considered at any photon impact energy. Due to this effect TDCS assumes the form $|T_1 + T_2|^2 + |W_1 + W_2|^2$, namely, in the overlap region, an ambiguity arises on whether the coincidence events stem from a click A of photoelectron 1 and a click B of Auger electron 1, or from a click A of photoelectron 2 and a click B of Auger electron 2. When under such conditions, the photon energy approaches $E_\gamma \approx 2E_1 - E_F \approx 2E_2 - E_F$, all three types of ambiguities are "activated," and the two-path TDCS must be calculated from the most general expression,

$$\frac{d^3\sigma}{d\epsilon_A d\Omega_A d\Omega_B} \propto \sum_{\sigma_A \sigma_B M_F} |T_1 - W_1 + T_2 - W_2|^2. \tag{6}$$

For targets selected here, the three cases listed by (5) can be clearly distinguished. The relevant TDCS expressions were published in two papers by Vegh and Macek [20] and Vegh [26]. They are presented below in a unified way and supplemented by expressions for reduced matrix elements in the single-configuration approximation. The model results are compared to the previously published coincidence and noncoincidence data. Finally, the expressions are integrated over solid angles of the both electrons and applied to the analysis of the experiment performed with MB-TOF.

In its fully decoupled form, the $|T_a \pm W_b|^2$ contribution to the TDCS is given by

$$\begin{aligned}
&\frac{d^3\sigma}{d\epsilon_A d\Omega_A d\Omega_B} \\
&= \frac{3C}{4\pi} \sum_{g_1 g_2 \kappa} \left\{ \left[\frac{B_a(g_1 g_2 \kappa) \hat{J}_a^2 \Gamma_a/(2\pi)}{(\epsilon_A - E_{\gamma a})^2 + \Gamma_a^2/4} \right.\right. \\
&\quad \left. + \frac{(-1)^\kappa B_b(g_2 g_1 \kappa) \hat{J}_b^2 \Gamma_b/(2\pi)}{(\epsilon_B - E_{\gamma b})^2 + \Gamma_b^2/4} \right] \mathcal{A}_{g_1 g_2 \kappa}(\Omega_A \Omega_B) \\
&\quad \left. \pm 2\mathrm{Re}\left[\frac{B_{ab}(g_1 g_2 \kappa) \hat{J}_a \hat{J}_b \sqrt{\Gamma_a \Gamma_b}/(2\pi) \mathcal{A}_{g_1 g_2 \kappa}(\Omega_A \Omega_B)}{(\epsilon_A - E_{\gamma a} - i\Gamma_a/2)(\epsilon_B - E_{\gamma b} + i\Gamma_b/2)} \right] \right\}.
\end{aligned} \tag{7}$$

The indices a and b may denote path 1 or 2 and the abbreviation $\hat{j}$ is used for $\sqrt{2j+1}$. The plain amplitudes squared, $|T_a|^2$ and $|W_b|^2$, are given by the first and the second term in the above expression, respectively, and the third term represents the exchange interference contribution. The products of bipolar spherical harmonics,

$$\Upsilon^{\kappa q}_{g_1 g_2}(\Omega_A \Omega_B) = \sum_{h_1 h_2} \langle g_1 h_1 g_2 h_2 | \kappa q \rangle Y_{g_1 h_1}(\Omega_A) Y_{g_2 h_2}(\Omega_B), \tag{8}$$

and of state dipoles $\rho_{\kappa q}(1,1)$ are summed up to obtain scalar invariants for a given type of excitation,

$$\mathcal{A}_{g_1 g_2 \kappa}(\Omega_A \Omega_B) = \sum_q \Upsilon^{\kappa q}_{g_1 g_2}(\Omega_A \Omega_B) \rho_{\kappa q}(1,1). \tag{9}$$

The components of the dipole photon statistical tensor are defined by the light polarization (described by Stokes parameters S_1, S_2, S_3) and by the selection of the quantization axis. The latter is generally chosen along the direction of the incident beam, and then the only nonvanishing tensor components are

$$\rho_{00} = \frac{1}{\sqrt{3}}, \quad \rho_{10} = \frac{S_3}{\sqrt{2}}, \quad \rho_{20} = \frac{1}{\sqrt{6}}, \quad \rho_{2\pm 2} = -\frac{S_1 \pm i S_2}{2}. \tag{10}$$

The weights $B_a(g_1 g_2 \kappa)$ of scalar invariants $\mathcal{A}_{g_1 g_2 \kappa}$ are expressed by summation of products of angular coupling coefficients (Clebsch-Gordan, $6j$, and $9j$ symbols) and reduced matrix elements over the orbital (l) and the total (j) angular momenta of partial waves for both electrons in the continuum:

$$\begin{aligned}
&B_a(g_1 g_2 \kappa) \\
&= \sum_{j_1 l_1 j_1' l_1'} \sum_{j_2 l_2 j_2' l_2'} (-1)^{j_1 + g_2 + J_F + J_a} \hat{j}_1 \hat{l}_1 \hat{j}_1' \hat{l}_1' \hat{j}_2 \hat{l}_2 \hat{j}_2' \hat{l}_2' \\
&\quad \times V^a_{l_2 j_2} V^{a*}_{l_2' j_2'} D^a_{l_1 j_1} D^{a*}_{l_1' j_1'} \langle l_1 0 l_1' 0 | g_1 0 \rangle \langle l_2 0 l_2' 0 | g_2 0 \rangle \\
&\quad \times \begin{Bmatrix} J_F & j_2 & J_a \\ g_2 & J_a & j_2' \end{Bmatrix} \begin{Bmatrix} l_1 & \frac{1}{2} & j_1 \\ j_1' & g_1 & j_1' \end{Bmatrix} \begin{Bmatrix} l_2 & \frac{1}{2} & j_2 \\ j_2' & g_2 & j_2' \end{Bmatrix} \begin{Bmatrix} j_1 & J_a & 1 \\ j_1' & J_a & 1 \\ g_1 & g_2 & \kappa \end{Bmatrix},
\end{aligned} \tag{11}$$

and

$$\begin{aligned}
&B_{ab}(g_1 g_2 \kappa) \\
&= \sum_{j_1 l_1 j_1' l_1'} \sum_{j_2 l_2 j_2' l_2'} (-1)^{J_a + J_F + g_1 + j_1 + j_1' - j_2} \\
&\quad \times \hat{j}_1 \hat{l}_1 \hat{j}_1' \hat{l}_1' \hat{j}_2 \hat{l}_2 \hat{j}_2' \hat{l}_2' V^a_{l_2 j_2} V^{b\,*}_{l_2' j_2'} D^a_{l_1 j_1} D^{b\,*}_{l_1' j_1'} \\
&\quad \times \langle l_1 0 l_2' 0 | g_1 0 \rangle \langle l_2 0 l_1' 0 | g_2 0 \rangle \begin{Bmatrix} l_1 & \frac{1}{2} & j_1 \\ j_2' & g_1 & l_2' \end{Bmatrix} \begin{Bmatrix} l_1' & \frac{1}{2} & j_1' \\ j_2 & g_2 & l_2 \end{Bmatrix} \\
&\quad \times \sum_x \hat{x}^2 \begin{Bmatrix} J_b & 1 & x \\ \kappa & j_1' & 1 \end{Bmatrix} \begin{Bmatrix} j_2 & g_1 & x \\ \kappa & j_1' & g_2 \end{Bmatrix} \begin{Bmatrix} j_1 & j_2' & g_1 \\ J_a & J_F & j_2 \\ 1 & J_b & x \end{Bmatrix}.
\end{aligned} \tag{12}$$

Finally, the reduced matrix elements are expressed within the single configuration model. In the simplest dipole (length) approximation, the photoionization amplitude for removing an nL_aJ_a electron from the atomic ground state ($J = 0$) is written as

$$\begin{aligned}
D^a_{lj}(E_\gamma) &= \langle k J_a [l\,(1/2)] j; 1 \| D \| 0 \rangle \\
&= 4\pi (-1)^{j + l - (1/2)} i^l e^{i\delta_l} \hat{j} \hat{l} \hat{J}_a \langle l 0 1 0 | L_a 0 \rangle \\
&\quad \times \begin{Bmatrix} j & 1 & J_a \\ L_a & \frac{1}{2} & l \end{Bmatrix} \int_0^\infty dr\, P_l(k; r) r P_{nL_a}(r),
\end{aligned}$$

where $P_l(k; r)$ represents the radial part of the partial wave of the continuum electron, normalized to $\delta^3(\mathbf{k}' - \mathbf{k})$ that enters the radial part $\mathcal{R}_{klnL_a}$ of the dipole integral with an initially occupied bound orbital P_{nL_a}. The partial wave phase at energy $\epsilon = k^2/2$ equals $\delta_l = \delta_l^c(1) + \Delta_l$ where $\delta_l^c(Z) =$

$\arg[\Gamma(1+l-Zi/k)]$ is the Coulomb phase, and Δ_l is an extra phase difference due to the short-range potential [37]. The reduced Auger matrix element is written as

$$V^a_{lj} = \langle k' J_F [l\,(1/2)] j; J_a \| V \| J_a \rangle = 4\pi i^l e^{i\sigma_l} \hat{J}_F \hat{L}_a \hat{S}_a \hat{j} \begin{Bmatrix} L_F & l & L_a \\ S_F & \frac{1}{2} & S_a \\ J_F & j & J_a \end{Bmatrix} \times \langle k'(L_F l) L_a, [S_F\,(1/2)] S_a \| V \| L_a S_a \rangle,$$

where $\sigma_l = \sigma^c_l(2) + \Delta'_l$ is the Auger scattering phase shift at electron energy $k'^2/2$. The reduced matrix elements for electrostatic interaction among the LS coupled states are expressed by a linear combination of the direct and the exchange Slater integrals involving four active orbitals [38].

An integration of the direct TDCS term $|T_a|^2$ over the solid angle of the Auger electron gives

$$\frac{d^2\sigma}{d\epsilon_A d\Omega_A} = \frac{3C\hat{J}_a^2}{\sqrt{4\pi}} \frac{\Gamma_a}{2\pi} \frac{\sum_{g_1 h_1} B_a(g_1 0 g_1) Y_{g_1 h_1}(\Omega_A) \rho_{g_1 h_1}}{\left[(\epsilon_A - E_{\gamma a})^2 + \Gamma_a^2/4\right] \sum_{l_2 j_2} \left| V^a_{l_2 j_2} \right|^2}. \tag{13}$$

For linearly polarized light, $S_1 = 1$, so that only ρ_{00}, ρ_{20} and $\rho_{22} = \rho_{2-2}$ components of the dipole statistical tensor are different from zero in the "beam" coordinate frame (10). The asymmetry parameter for channel a is expressed as

$$\beta^a_{\rm ph} = \frac{B_a(202)\rho_{22}\sqrt{40/3}}{B_a(000)\rho_{00} - B_a(202)[\rho_{20}\sqrt{5/4} + \rho_{22}\sqrt{5/6}]}, \tag{14}$$

with weights B_a depending on photon impact energy. If the quantization axis is chosen along the light polarization, only $\rho_{00} = 1/\sqrt{3}$ and $\rho_{20} = -2/\sqrt{6}$ are different from zero, and (14) turns out particularly simple:

$$\beta^a_{\rm ph} = -\sqrt{10}\frac{B_a(202)}{B_a(000)}. \tag{15}$$

As the "interference" angular weights $B_{ab}(000)$ and $B_{ab}(202) = B^*_{ab}(022)$ are different from zero, $\beta^a_{\rm ph}$ changes in the vicinity of the critical photon energies: when the exchange interference condition is exactly fulfilled ($E_\gamma = E^c_\gamma$), $\beta^a_{\rm ph}$ turns into

$$\beta^{ab} = -\sqrt{10}\frac{\frac{\hat{J}_a^2}{\Gamma_a} B_a(202) + \frac{\hat{J}_b^2}{\Gamma_b} B_b(022) - 2\frac{\hat{J}_a \hat{J}_b}{\sqrt{\Gamma_a \Gamma_b}} {\rm Re} B_{ab}(202)}{\frac{\hat{J}_a^2}{\Gamma_a} B_a(000) + \frac{\hat{J}_b^2}{\Gamma_b} B_b(000) - 2\frac{\hat{J}_a \hat{J}_b}{\sqrt{\Gamma_a \Gamma_b}} B_{ab}(000)}. \tag{16}$$

The TDCS integrated over the photoelectron angle is obtained from Eqs. (15) and (16) by exchanging $B(202)$ with $B(022)$: the asymmetry parameter of the Auger electron is then

$$\beta^a_{\rm Au} = -\sqrt{10}\frac{B_a(022)}{B_a(000)}, \tag{17}$$

which turns into

$$\beta^{ba} = -\sqrt{10}\frac{\frac{\hat{J}_a^2}{\Gamma_a} B_a(022) + \frac{\hat{J}_b^2}{\Gamma_b} B_b(202) - 2\frac{\hat{J}_a \hat{J}_b}{\sqrt{\Gamma_a \Gamma_b}} {\rm Re} B_{ab}(022)}{\frac{\hat{J}_a^2}{\Gamma_a} B_a(000) + \frac{\hat{J}_b^2}{\Gamma_b} B_b(000) - 2\frac{\hat{J}_a \hat{J}_b}{\sqrt{\Gamma_a \Gamma_b}} B_{ab}(000)} \tag{18}$$

at the critical photon energy. Note that $\beta^{ab} \neq \beta^{ba}$ when the interchannel exchange interference condition applies ($a \neq b$). However, the observed change of the asymmetry parameter due to the exchange interference is expected to be less than $\beta^a \to \beta^{ab}$, because the (predominant) signal of the concurrent noninterfering decay channels associated with the selected photoelectron remains unchanged. Let σ^i denote the photoionization cross section and $\mathcal{B}^i$ the Auger branching ratio of channel i to the selected final state. The expected asymmetry parameter is then

$$(\beta^{ab})' = \frac{(\sigma^a \mathcal{B}^a + \sigma^b \mathcal{B}^b)\beta^{ab} + \sigma^a(1 - \mathcal{B}^a)\beta^a_{\rm ph}}{\sigma^a + \sigma^b \mathcal{B}^b}. \tag{19}$$

In focus of this paper are the exchange interference effects in the angle-integrated cross section. The decisive factors here are the angular weights $B(000)$ as all the other contributions to the cross section integrate out:

$$\frac{d\sigma}{d\epsilon_A} = \frac{3C\rho_{00}}{2\pi}\left[\frac{B_a(000)\hat{J}_a^2\Gamma_a}{(\epsilon_A - E_{\gamma a})^2 + \Gamma_a^2/4} + \frac{B_b(000)\hat{J}_b^2\Gamma_b}{(\epsilon_B - E_{\gamma b})^2 + \Gamma_b^2/4} \pm 2B_{ab}(000)\hat{J}_a\hat{J}_b \frac{\sqrt{\Gamma_a\Gamma_b}[(\epsilon_A - E_{\gamma a})(\epsilon_B - E_{\gamma b}) + \Gamma_a\Gamma_b/4]}{[(\epsilon_A - E_{\gamma a})^2 + \Gamma_a^2/4][(\epsilon_B - E_{\gamma b})^2 + \Gamma_b^2/4)]}\right]. \tag{20}$$

In this case, the interference effect depends on the ratio of the corresponding angular weight,

$$B_{ab}(000) = \sum_{j_1 l_1 j_2 l_2} \frac{(-1)^{1+J_a+J_b+j_2-j_1}}{\sqrt{3}} \begin{Bmatrix} J_a & J_F & j_2 \\ J_b & 1 & j_1 \end{Bmatrix} V^a_{l_2 j_2} V^{b*}_{l_1 j_1} D^a_{l_1 j_1}(E^c_\gamma) D^{b*}_{l_2 j_2}(E^c_\gamma), \tag{21}$$

with respect to

$$B_a(000) = \frac{1}{\sqrt{3}\hat{J}_a^2} \sum_{j_1 l_1 j_2 l_2} \left| V^a_{l_2 j_2} \right|^2 \left| D^a_{l_1 j_1}(E^c_\gamma) \right|^2. \tag{22}$$

The $B_a(000)$ weights give an incoherent contribution to the cross section and determine the total cross section for photoinduced Auger decay:

$$\sigma_F = C \sum_a \sum_{j_1 l_1 j_2 l_2} \left| V^a_{l_2 j_2} \right|^2 \left| D^a_{l_1 j_1}(E_\gamma) \right|^2. \tag{23}$$

Finally, the total inner-hole photoionization cross section is given by

$$\sigma = \sigma^1 + \sigma^2 = C \sum_a \sum_{j_1 l_1} \left| D^a_{l_1 j_1}(E_\gamma) \right|^2. \tag{24}$$

The cross sections are converted to atomic units by the factor $C = (4/3)\pi^2 \alpha k E_\gamma$ [39].

A. Kr $M_{4,5}$–N_1O_{23} and Xe $N_{4,5}$–O_1O_{23} parametrization and model testing

In the single configuration approximation, p and f waves are activated to describe both the photoelectron and Auger electron emitted in the Kr $M_{4,5}$–N_1N_{23} and Xe $N_{4,5}$–O_1O_{23} decay. Relying on the relatively weak energy dependence of the reduced matrix elements in a few-eV-wide energy region of interest, the energies $\epsilon = k^2/2$ of both electrons were fixed to 38.1 and 20.7 eV for the Kr and Xe case, respectively. The photoelectron continuum waves and the dipole radial matrix elements were calculated with the ground-state optimized orbitals, and for the Auger decay, the optimized orbitals of the ionic nd^{-1} configuration were employed [40]. The following parameter values were obtained:

Kr

$$\begin{aligned}
&\mathcal{R}_{kp3d} = 0.079, \quad \mathcal{R}_{kf3d} = 0.206,\\
&\langle k(1p)2,[0\ (1/2)](1/2)\|V\|2\ (1/2)\rangle = 0.0073,\\
&\langle k(1f)2,[0\ (1/2)](1/2)\|V\|2\ (1/2)\rangle = -0.0132,\\
&\delta_p = 6.38, \quad \delta_f = -0.13,\\
&\sigma_p = 4.83, \quad \sigma_f = -1.02,
\end{aligned} \tag{25}$$

Xe

$$\begin{aligned}
&\mathcal{R}_{kp4d} = 0.189, \ \mathcal{R}_{kf4d} = -0.655,\\
&\langle k(1p)2,[0\ (1/2)](1/2)\|V\|2\ (1/2)\rangle = 0.0131,\\
&\langle k(1f)2,[0\ (1/2)](1/2)\|V\|2\ (1/2)\rangle = 0.0272,\\
&\delta_p = 9.05, \quad \delta_f = -0.42,\\
&\sigma_p = 6.91, \quad \sigma_f = -1.07.
\end{aligned} \tag{26}$$

As demonstrated above, the angular weights $B(g_1g_2\kappa)$ at given photon impact and electron emission energies determine the TDCS and the other differential cross sections of the lower order. In both examined cases, the largest index of angular weights is 6 and, as presented in Fig. 2, there are altogether 13 different combinations of $g_1g_2\kappa$ that result in nonvanishing angular weights, either for the direct (11) or for the interference contribution (12).

To test the parameter values, we have calculated asymmetry parameter β for the Kr $3d$ photoelectron at 132.6 eV photon impact energy: our value of -0.07 is in good agreement with the experimental observations [41]. The calculated alignment parameter A_{20} comes out as -0.26 and -0.24, for the $3d_{5/2}$ and the $3d_{3/2}$ hole, respectively [42], and the corresponding angular anisotropy parameter $\alpha_2 = \beta_{\mathrm{Au}}/A_{20}$ for Auger decay into the $(4s4p)^{-1}\,{}^1P_1$ state is -0.63 and -0.59, in reasonable agreement with the experimental data [42] and other calculations [43,44].

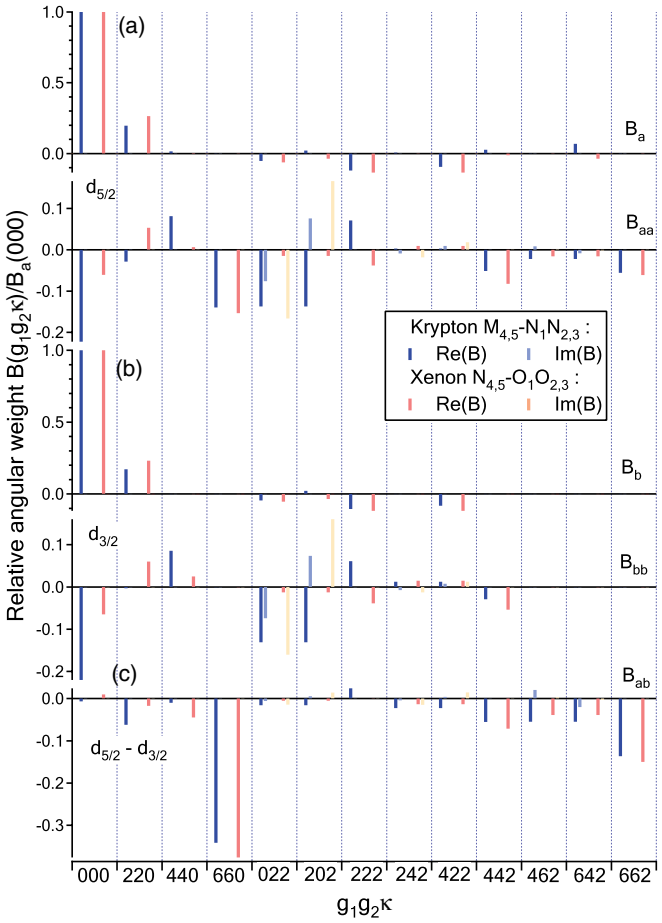

FIG. 2. (Color online) Relative angular weights $B(g_1g_2\kappa)/B_a(000)$ of the direct and exchange interference contribution to TDCS calculated using Eqs. (11) for (a) path 1 ($d_{5/2}$), (b) path 2 ($d_{3/2}$). (c) Angular weights of $d_{5/2}$–$d_{3/2}$ intrachannel exchange interference calculated by Eq. (12). Blue (black) and red (gray) bars denote calculated weights at photon energy 132.6 and 89.0 eV for Kr and Xe, respectively. Double bar denotes real (left) and imaginary (right) component of the weight.

For the Xe $4d$ photoelectron at 89 eV photon energy, the calculated asymmetry parameter of $+0.11$ agrees well with the experimental value [45]. The alignment parameter A_{20} of $4d_{5/2}$ and $4d_{3/2}$ hole is calculated to be -0.24 and -0.23, respectively, in good agreement with [46,47]. The angular anisotropy parameter for Xe^{2+} $(5s5p)^{-1}\,{}^1P_1$ final state is -0.81 and -0.76 for the $4d_{5/2}$ and the $4d_{3/2}$ hole, respectively, in reasonably good agreement with the results of Tulkki *et al.* [44]. At 20.7 eV photoelectron energy the p-to-f partial $4d$ photoionization cross-section ratio is calculated to be 0.055, similar to the value reported previously [48]. A fast rise of photoionization cross section above the Xe $4d$ ionization threshold is due to the shape resonance in the f-wave channel. Our value $\sigma(89\ \mathrm{eV}) \approx 23.8$ Mb is in reasonable agreement with previously published data [49,50]. The calculated branching ratio of 0.14 for the selected Auger decay that gives rise to the well isolated Auger line at 19.67 eV (or at 21.65 eV) is consistent with the observed value of 0.10–0.15 [51]. Although a strong configuration interaction

in the final doubly charged states leads to the rich $N_{4,5}$–O_1O_{23} spectrum [52], it is still mainly the weight of the $(5s5p)^{-1}$ configuration that determines the cross-section behavior. The effects of various approximations for the description of the Auger spectra are discussed in [44].

A further test of the model is provided by the experimental TDCS results of Rioual *et al.* [29] for Kr and Selles *et al.* [25] for Xe and by our results for Xe. The first group reported an observation of interchannel exchange interference effect in $(\gamma,2e)$ reaction mediated by the Kr^+ $3d_{5/2,3/2}$ pair of states. The multicoincidence chamber at the Gas Phase Photoemission beamline at Elettra synchrotron was set to detect one electron along the polarization direction of light, and the angular distribution of the coincident electron was measured by an independent electron spectrometer in the plane perpendicular to the photon beam. At 132.15-eV photon energy (out-of-interference condition), the spectrometer energies were tuned to measure the 3/2 Auger electron and the 5/2 photoelectron angular distribution, both leading to the $Kr^{2+}(4s4p)^{-1}\,{}^1P_1$ final state. These results were compared to the ones measured at the critical photon energy with the two spectrometers tuned to the energies of the 3/2 photoelectron and the 5/2 Auger electron, respectively. The TDCS was shown to deviate substantially from the sum of the two out-of-interference data sets. As shown in Fig. 3(a), our model definitely confirms the interpretation given by the authors and predicts intrachannel exchange effect in the angular distribution for both the $3d_{5/2}$ and the $3d_{3/2}$ holes.

The experiment from Ref. [25] deals with the angular intrachannel exchange interference effect, and a part of the published data is presented in Fig. 4(a). The TDCS signal for the reaction mediated by the Xe^+ $4d_{5/2}$ state was measured at two different photon energies: 87.0 eV, the critical energy for interchannel exchange interference leading to the Xe^{2+} $(5s5p)^{-1}\,{}^1P_1$ final state, and at 1.0 eV lower photon energy. One of the electrons was detected along the light polarization axis and the other was detected by a toroidal analyzer in the plane perpendicular to the photon beam. An extra increase of the coincidence yield prominent for the back-to-back electron emission was interpreted as an effect of the exchange interference within the 5/2 decay channel. Such an explanation was supported by the calculations of the TDCS based on the matrix element ratios and phase differences extracted from the previously measured asymmetry parameter values. A good agreement of our *ab initio* calculations with the previous experimental data fully confirms this conclusion. Our calculations in Fig. 4(c) also show that the effect of exchange interference for the 3/2 path (case number 6 in Table I) is expected to be less prominent than for the 5/2 path (number 3). On the contrary, the effect of the 3/2-5/2 intrachannel exchange interference is predicted to be the most prominent in the angle-resolved signal (4 and 5), which is related to the relatively large values of $B_{ab}(660)$ and $B_{ab}(662)$ angular weights (Fig. 2). This is confirmed by our $(\gamma,2e)$ experimental results presented in Fig. 4(b).

When the same partial wave l is dominant in both the photoionization cross section and the Auger partial decay rate, it is possible to obtain a rough estimate of the exchange interference effect in the angle-integrated spectrum. Within the single configuration approximation, the ratio of the "interference" angular weight versus the "direct" angular weight may be expressed in a relatively simple manner,

$$\frac{B_{ab}(000)}{B_a(000)} = (-1)^{J_a+J_b+1}\hat{j}_a^2\hat{j}_b^2\left(\sum_{j_1 j_2=l\pm1/2}\hat{j}_1^2\hat{j}_2^2\begin{Bmatrix} J_a & J_F & j_2\\ J_b & 1 & j_1\end{Bmatrix}\begin{Bmatrix} j_1 & 1 & J_a\\ L & \frac{1}{2} & l\end{Bmatrix}\begin{Bmatrix} j_2 & 1 & J_b\\ L & \frac{1}{2} & l\end{Bmatrix}\begin{Bmatrix} L_F & l & L\\ S_F & \frac{1}{2} & S\\ J_F & j_2 & J_a\end{Bmatrix}\begin{Bmatrix} L_F & l & L\\ S_F & \frac{1}{2} & S\\ J_F & j_1 & J_b\end{Bmatrix}\right)$$
$$\Big/\left(\sum_{j=l\pm1/2}\hat{j}^2\begin{Bmatrix} j & 1 & J_a\\ L & \frac{1}{2} & l\end{Bmatrix}^2\times\sum_{j=l\pm1/2}\hat{j}^2\begin{Bmatrix} L_F & l & L\\ S_F & \frac{1}{2} & S\\ J_F & j & J_a\end{Bmatrix}^2\right), \tag{27}$$

using only angular momenta that define path(s) mediated by the ${}^2L_{J_a}$ and/or ${}^2L_{J_b}$ hole(s). For Xe $4d_{5/2,3/2}^{-1}$, the ff partial wave combination gives the largest contribution to the photoinduced N_{23}–O_1O_{23} Auger cross section. Selecting ${}^1P_0$ for the final state the above equation gives

$$\frac{B_{3/2,3/2}}{B_{3/2}} = -\frac{1}{15},\quad \frac{B_{5/2,5/2}}{B_{5/2}} = -\frac{19}{315},\quad \frac{B_{5/2,3/2}}{B_{5/2}} = \frac{2}{105}\sqrt{\frac{2}{3}}. \tag{28}$$

Most of the remaining discrepancy with the results of more accurate calculation (Table II) is attributed to the missing pf and fp contributions in the numerator of Eq. (27). Further comparison shows that the single partial wave approximation is not reliable for the Kr $3d_{5/2,3/2}^{-1}$ case—the ratio of angular weights for an intrachannel exchange interference is several times larger than the predictions (28).

B. PCI correction

In these experiments pairs of electrons with close energies are emitted. One thus needs to estimate the effect of the postcollision interaction on the multidifferential cross sections presented above. Due to PCI, electron energies and emission angles are redistributed, i.e., spectral line shapes are distorted and the probability for ejection of both electrons into the same narrow solid angle is decreased when electrons are emitted with about the same energy. The PCI framework presented by Sheinerman and Schmidt [53] and proved by Rouvellou *et al.* [54] for the case of the intrachannel exchange interference in Auger decay of Ne $^+(2s2p)^{-1}3p$ satellite state presents a

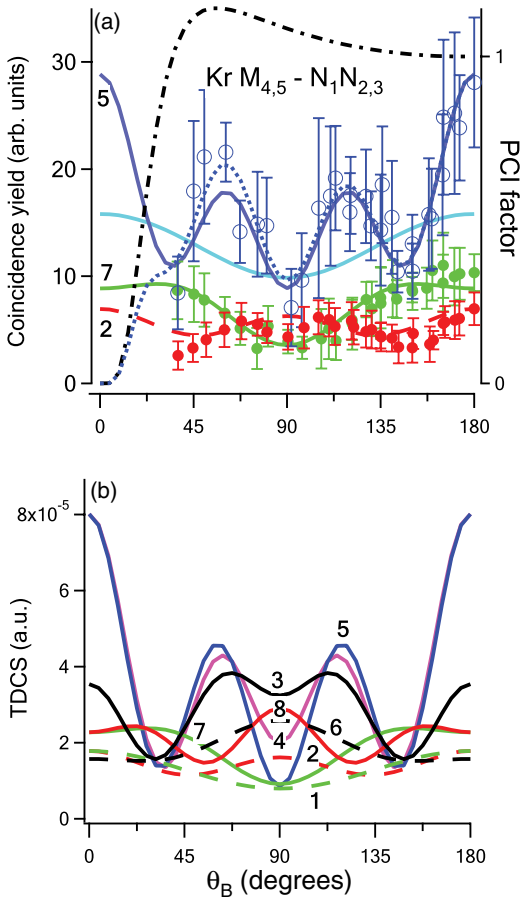

FIG. 3. (Color online) The $(\gamma,2e)$ angular distributions for the Kr $3d_{5/2,3/2}$ case. One electron is emitted along the polarization direction of the incident light ($\theta_A = 0$) and the other at an angle θ_B with respect to the first electron. (a) Experimental result of Rioual *et al.* [29] for the $\mathrm{Kr}(4s4p)^{-1}$ final state [Figs. 2(a), 2(b), and 3 in [29]] compared to our model result with the experimental broadening included (6° angular resolution and 120 meV energy resolution). The curves are numbered according to the spectrometer energy settings presented in Table I. The black (blue) curve and black (blue) points represent the angular distribution when the interchannel exchange interference condition is fulfilled, and the gray (light blue) line simulates the same case without the interference term. The dot-dashed black line represents the PCI factor, and the (blue) dotted line is a PCI-corrected angular distribution. (b) The calculated nonconvoluted angular distributions for the Kr experimental settings are given in Table I.

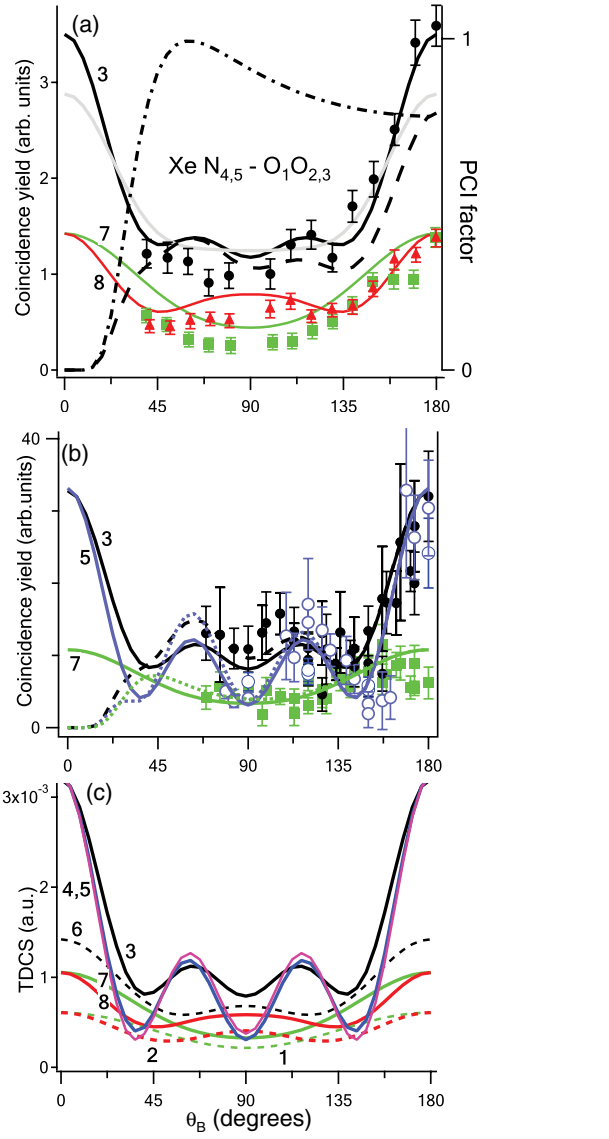

FIG. 4. (Color online) The $(\gamma,2e)$ angular distributions for the Xe $4d_{5/2,3/2}$ case. (a) Experimental result of Selles *et al.* [25] for the Xe $(5s5p)^{-1}$ final state [Figs. 2(a)–2(c) in [25]] compared to our model result with experimental broadening included (10° angular sectors and 200-meV energy resolution). The black dash-dotted curve denotes the PCI correction factor, the black dashed curve is the PCI-corrected cross section, and the gray curve gives model result 3 without interference and PCI effects included. (b) Our experimental results compared to the model result (full lines: without PCI; dashed line: PCI corrected). (c) The calculated nonconvoluted angular distributions without PCI factor enumerated for the Xe experimental settings (Table I).

possible way to introduce PCI into the model. The amplitude correction is done by the PCI factor $R(\epsilon_A,\epsilon_B,\theta_{AB},\Gamma_a)$ that depends on the electron energies, the interelectron angle θ_{AB}, and time delay in the electron emission, indicated by the lifetime $1/\Gamma_a$:

$$R_{ABa} = e^{-\pi\xi/2}\Gamma(1-a)\Gamma(b)\left(\epsilon_A - E_{\gamma a} + i\frac{\Gamma_a}{2}\right)^{1-b} \times {}_2F_1(a,b,1,z), \tag{29}$$

where

$$\xi = \xi_{AB} + \xi_{AC} - \xi_{AD}, \quad \xi_{ij} = Z_iZ_j/v_{ij} \tag{30}$$

is expressed by the charges (Z_i,Z_j) and magnitudes of relative velocities $\mathbf{v}_{ij} = \mathbf{v}_i - \mathbf{v}_j$ of particles in the intermediate $(A+D)$ and final state $(A+B+C)$. The parameters of the full hypergeometric function ${}_2F_1$ are given by

$$a = -i\xi_{AB}, \quad b = 1 + i(\xi_{AC} - \xi_{AD}),$$
$$z = -\frac{K_{AB}\kappa/\mu_{AD} + \mathbf{K}_{AB}\cdot\mathbf{v}_{AD}}{\epsilon_B - E_{aF} + i\Gamma_a/2}, \tag{31}$$
$$\kappa = \sqrt{2E_{\gamma a} + i\Gamma_a}, \ \mathbf{K}_{AB} = \tfrac{1}{2}\mathbf{v}_{AB}.$$

TABLE I. Photon energies (E_γ) and electron energies (ϵ_A,ϵ_B) selected to study the effect of exchange interferences in the photoinduced Kr $M_{4,5}$–$N_1N_{2,3}$ and Xe $N_{4,5}$–$O_1O_{2,3}$ decay. The last column reports the asymmetry parameter β_A for an angular distribution of the electron with energy ϵ_A, integrated over an angle of the other electron. Abbreviations ph (photoelectron) and Au (Auger electron) denote the origin of an electron detected at $\theta_A = 0$.

#	E_γ (eV)	Channel	Interference?	ϵ_A (eV)	$\theta_A = 0$	ϵ_B (eV)	β_A
Kr							
1	131.36	3/2	no	36.32	ph	38.71	−0.07
2	131.36	3/2	no	38.71	Au	36.32	+0.14
3	131.36	5/2	yes	37.57	ph-Au	37.57	−0.32
4	132.61	3/2,5/2	yes	37.57	ph-Au	38.82	+0.02
5	132.61	5/2,3/2	yes	38.82	ph-Au	37.57	−0.03
6	133.86	3/2	yes	38.82	ph-Au	38.82	−0.32
7	133.86	5/2	no	40.07	ph	38.82	−0.07
8	133.86	5/2	no	38.82	Au	40.07	+0.14
Xe							
1	86.95	3/2	no	17.45	ph	21.45	+0.11
2	86.95	3/2	no	21.45	Au	17.45	+0.17
3	86.95	5/2	yes	19.45	ph-Au	19.45	+0.10
4	88.95	3/2,5/2	yes	19.45	ph-Au	21.45	+0.14
5	88.95	5/2,3/2	yes	21.45	ph-Au	19.45	+0.12
6	90.95	3/2	yes	21.45	ph-Au	21.45	+0.10
7	90.95	5/2	no	23.45	ph	19.45	+0.11
8	90.95	5/2	no	19.45	Au	23.45	+0.20

The PCI amplitude is easily incorporated into the TDCS formula (7):

$$\frac{d^3\sigma_{PCI}}{d\epsilon_A d\Omega_A d\Omega_B} = |T_a|^2|R_{ABa}|^2 + |W_b|^2|R_{BAb}|^2 \pm 2\mathrm{Re}(T_a^* W_b)\mathrm{Re}(R_{ABa}^* R_{BAb}) \times \left[1 - \frac{\mathrm{Im}(T_a^* W_b)\mathrm{Im}(R_{ABa}^* R_{BAb})}{\mathrm{Re}(T_a^* W_b)\mathrm{Re}(R_{ABa}^* R_{BAb})}\right]. \quad (32)$$

Since the R_{ABa} depends on the interelectron angle θ_{AB} as well as on electron energies, the energy dependence of the cross section is not decoupled anymore from its dependence on θ_{AB}. However, the previous decomposition into scalar invariants may still be useful. Namely, for critical photon energies with electron energies close to the resonant values, $R_{ABa} \approx R_{BAb}$, so that $\mathrm{Re}(R_{ABa}^* R_{BAb}) \approx |R_{ABa}|^2 \approx |R_{BAb}|^2$. At the same time, the ratio in Eq. (32) is much smaller than 1 so that

$$\frac{d^3\sigma_{PCI}}{d\epsilon_A d\Omega_A d\Omega_B} \approx |R_{ABa}|^2 \frac{d^3\sigma}{d\epsilon_A d\Omega_A d\Omega_B}. \quad (33)$$

As seen in Figs. 3 and 4, the effect of the PCI factor $|R_{ABa}|^2$ is to suppress the cross section for small interelectron angles, while for $\theta_{AB} > \pi/4$, the TDCS shape is practically unaffected by postcollision interaction.

TABLE II. Calculated "isotropic" angular weights $B_a(000)$ and $B_{ab}(000)$ in a.u. for the Kr$3d_{5/2,3/2}^{-1}$ and Xe$4d_{5/2,3/2}^{-1}$ intermediate states at 132.6 and 89.0 eV photon energy, respectively. The final states are the Kr $(4s4p)^{-1}\,{}^1P$ and the Xe $(5s5p)^{-1}\,{}^1P$ state.

	$B_{5/2} = B_{3/2}$	$B_{5/2,5/2}$	$B_{3/2,3/2}$	$B_{5/2,3/2}$
Kr	+2.20	−0.49	−0.48	−0.01
Xe	+38.15	−2.32	−2.47	+0.38

Instead of using the approximation (33), one may directly recalculate the weights for the cross section with PCI factor included (32). The drawback is that the new scalar invariants become energy dependent, i.e., their values may change substantially across the spectral line. This more general approach could be useful for the interpretation of coincidence spectra taken at similar electron energies and small interelectron angles [54]: the PCI factor is first expanded into scalar bipolar harmonics,

$$|R_{ABa}|^2 = 4\pi \sum_l (-1)^g \sqrt{\hat{g}} A_g(\epsilon_A) \Upsilon_{gg}^{00}(\Omega_A \Omega_B), \quad (34)$$

and then the products of bipolar spherical harmonics that appear in the TDCS expression are contracted according to

$$\Upsilon_{g_1 g_2}^{\kappa 0} \Upsilon_{gg}^{00} = \frac{(-1)^\kappa}{4\pi} \sqrt{\hat{g}_1 \hat{g}_2 \hat{g}} \sum_{p_1 p_2} \left[\sqrt{\hat{p}_1 \hat{p}_2} \begin{pmatrix} g_1 & g & p_1 \\ 0 & 0 & 0 \end{pmatrix} \times \begin{pmatrix} g_2 & g & p_2 \\ 0 & 0 & 0 \end{pmatrix} \begin{Bmatrix} p_1 & p_2 & \kappa \\ g_2 & g_1 & g \end{Bmatrix} \Upsilon_{p_1 p_2}^{\kappa 0}\right]. \quad (35)$$

With the PCI functions, given by

$$A_g(\epsilon_A) = \frac{1}{2} \int_0^\pi d\theta \sin\theta P_g(\cos\theta) \times |R_{ABa}(\epsilon_A, E_{\gamma F} - \epsilon_A, \theta, \Gamma_a)|^2, \quad (36)$$

the new TDCS weights $\tilde{B}_a(g_1' g_2' \kappa)$ can be easily constructed from the known weights $B_a(g_1 g_2 \kappa)$ for each of the three terms of the cross section. The lower order cross sections are then extracted from $\tilde{B}_a$ weights as described above. The indices g_1', g_2' are still even, with their cutoff values depending on the number of A_g terms taken to represent the PCI factor in (34).

It is interesting to consider the PCI effect in coincidence spectra, integrated over the solid angle of *one* of the electrons in the pair. The photoelectron angular distribution can be cast into the folowing form:

$$\frac{d^2\sigma_{PCI}}{d\epsilon_A d\Omega_A} = \sigma_0(\epsilon_A)\left[1 + \sum_{g=2,4,\ldots} \beta_g(\epsilon_A) P_g(\cos\theta_A)\right], \quad (37)$$

where

$$\sigma_0 = 3C\hat{J}_a^2 \frac{\Gamma_a}{2\pi} \frac{\beta_0(\epsilon_A)}{\left[(\epsilon_A - E_{\gamma a})^2 + \Gamma_a^2/4\right] \sum_{l_2 j_2} \left|V^a_{l_2 j_2}\right|^2}, \quad (38)$$

$$\beta_0 = \sum_g A_g(\epsilon_A) \sum_{\kappa=0,2} \rho_{\kappa 0} \langle g 0 g 0 | \kappa 0\rangle B_a(gg\kappa),$$

$$\beta_{g>0} = \frac{1}{\beta_0(\epsilon_A)} \sum_{g_1 \leqslant g_2} \left[\left(1 - \frac{\delta_{g_1 g_2}}{2}\right)\sqrt{\hat{g}_1 \hat{g}_2}\langle g_1 0 g_2 0 | g 0\rangle^2 \times \sum_{\kappa=0,2} (\rho_{\kappa 0}\langle g_1 0 g_2 0 | \kappa 0\rangle [B_a(g_1 g_2 \kappa) A_{g_2}(\epsilon_A) + B_a(g_2 g_1 \kappa) A_{g_1}(\epsilon_A)])\right]. \quad (39)$$

When $|R_{ABa}|^2 = 1$, only $A_0 = 1$ is different from zero and Eq. (37) turns into the familiar $1 + \beta_{\rm ph} P_2(\cos\theta_A)$ form of angular distribution, as discussed above. PCI effect causes the shape of the angular distribution to depend on electron energy ϵ_A via the $A_{g_2}(\epsilon_A)$ PCI functions entering expressions for the asymmetry parameters β_g together with the weights $B_a(g_1 g_2 \kappa)$. The five asymmetry parameters β_2, β_4, β_6, β_8, β_{10} are nonzero for the $d_{5/2}$ channel in the studied Kr and Xe cases because the nonzero weight with the highest indices $g_1 g_2$ is $B_a(642)$. Consequently, three $A_{g_2}(\epsilon_A)$ functions are activated and the importance of PCI is indicated by the relative magnitudes of $1 - A_0$, A_2, and A_4 versus 1.

To demonstrate the PCI effect on the line shapes and the angular distributions of the photoelectron and the Auger electron, the five asymmetry parameters are presented in Fig. 5 as a function of electron energy for Xe. PCI is expected to introduce an energy shift of 15 meV and some asymmetry for both line profiles [Fig. 5(a)]. The data for the Auger line were obtained after expanding $|R_{BAa}|^2$ according to (36) and using the corresponding PCI functions in Eq. (38) with A_{g_1} and A_{g_2} interchanged. The same formula can be adapted for the exchange interference conditions in a straightforward manner by taking care about using proper weights, energy denominators, and PCI factors for the exchange and the exchange interference terms [Fig. 5(b)]. It is evident that the angular distribution is expected to be slightly different on the low- and the high-energy tail of either of the spectral lines, as shown in Fig. 5(c) for the exchange interference conditions. One must be aware that proper simulation of an angle dependent PCI effect on the photoelectron line in the *noncoincidence* measurements must include PCI with Auger electrons leading to *all* final dication states. It is also clear that both, PCI and the exchange interference need to be considered to reconstruct the angular distribution. On the other hand, the exchange interference mainly affects the intensity of the angle

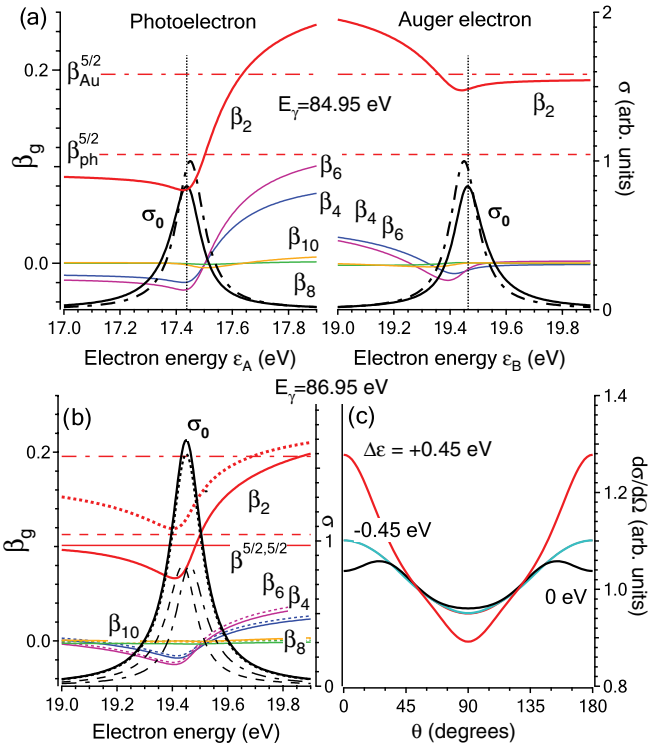

FIG. 5. (Color online) (a) Calculated asymmetry parameters β_g (37) for Xe $4d_{5/2}$ photoelectron and Auger electron corresponding to Xe $(5s5p)^{-1}\,{}^1P$ final state out of the exchange interference conditions. An angle integrated cross section σ_0 (black full line) is compared to the corresponding non-PCI cross section (black dot-dashed line). The non-PCI asymmetry parameters $\beta_{\rm ph}^{5/2} = 0.113$ (15) and $\beta_{\rm Au}^{5/2} = 0.196$ (17) are also shown. (b) PCI asymmetry parameters for photon energy set for the intrachannel exchange interference (full lines). The non-PCI asymmetry parameter is $\beta^{5/2,5/2} = 0.101$. PCI parameters with no exchange interference contribution are shown by dotted lines. σ_0 is denoted by the black line and the dotted black line presents the PCI cross section without the interference term (the sum of black dashed lines). (c) Calculated angular distribution at the top of the peak in (b) (black line, $\Delta\epsilon = 0$ eV), and at $\Delta\epsilon = \pm 0.45$ eV electron energy detuning (intensity $\times 34$).

integrated cross section σ_0. This can be seen by comparing the result in Fig. 5(b) and the non-PCI result in Fig. 6 below: in both cases, the exchange interference leads to about 6% increase of the maximum line intensity. The smallness of PCI effect is evidenced also by symmetric line shapes of spectral lines in Figs. 6 and 7. PCI effects will therefore be neglected in the following section dealing with angle integrated spectra.

IV. COMPARISON WITH ANGLE-INTEGRATED EXPERIMENTAL DATA

The signs and relative magnitudes of isotropic interference weights $B_{ab}(000)$ with respect to $B_a(000)$ in Table II indicate that due to the intrachannel exchange, about 20% (6%) increase of the coincidence yield is expected at the critical photon energy at the maximum of the spectral line for Kr (Xe). The calculation shows that the effect of interchannel exchange is considerably smaller, it amounts to only about 1% spectral line intensity change for Kr and Xe. As demonstrated

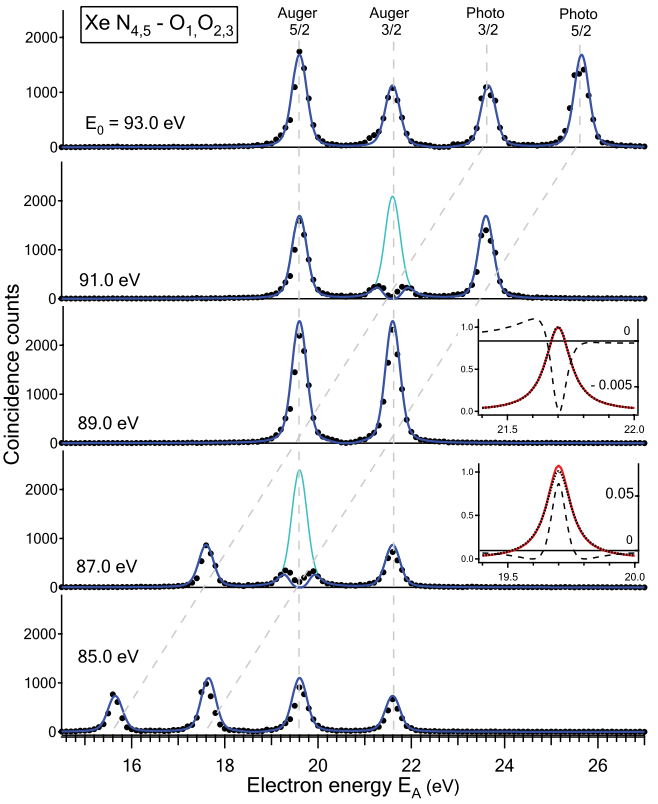

FIG. 6. (Color online) Projection of the coincidence yield measured in 10 min on a single energy axis (black circles) compared to the calculated $C_F(E_A;E_\gamma)$ for the Xe $(5s5p)^{-1}\,{}^1P$ final state (41). The solid black (blue) line represents the result with the nonzero detector dead time and the light gray (light blue) line represents the result with the dead time zero. The two insets show the difference in spectral shapes (dashed line, right axis) with interference switched on [red (gray) line] and off (black line) when the lines are broadened only by their natural linewidth (0.12 eV): the lower inset applies for the intrachannel exchange interference (5/2 channel) and the upper one for the 5/2–3/2 interchannel exchange interference.

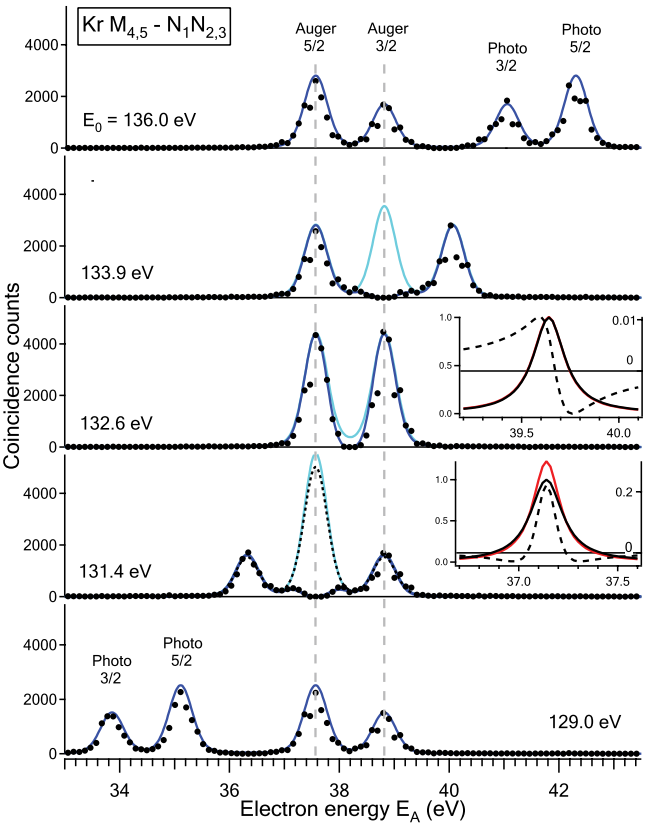

FIG. 7. (Color online) Projection of the measured coincidence yield on a single energy axis (black circles) compared to $C_F(E_A;E_\gamma)$, calculated by Eq. (41) for the Kr $(4s4p)^{-1}\,{}^1P$ final state (41). The solid black (blue) line represents the result that takes into account the dead time of the detector. The light gray (light blue) line represents the model result without the dead-time effect, and the dotted black line the model result without the dead-time effect and without the interference term. The two insets show the difference of spectral shapes (dashed line, right axis) with interference switched on (red line) and off (black line) when the lines are broadened only by their natural linewidth of 98 meV: the lower inset applies for the intrachannel exchange interference (5/2 channel) and the upper one for the 5/2–3/2 interchannel exchange interference.

in Figs. 7 and 6, a finite experimental energy resolution makes the signal contrast worse since the energy convolution tends to smear out the interference effect. We look for the fingerprint of the interference effect in a sequence of experimental energy maps (E_A,E_B) recorded at different incoming photon energies. The model cross sections are convoluted with experimental (Gaussian) transmission function $G(x-x_0,\text{full width at half maximum})$ for both detected electrons:

$$\mathcal{C}_F = \int_{E_A-\Delta_A}^{E_A+\Delta_A} d\epsilon_A\, G_A(\epsilon_A - E_A, s_A) G_B \times (E_{\gamma F} - \epsilon_A - E_B, s_B)\frac{d\sigma}{d\epsilon_A}. \quad (40)$$

The integration range is given by $\pm\Delta_A$, equal to a few times the width s_A of the Gaussian transmission function of spectrometer A. A meeting ground with the experiment is a projection of coincidence counts $\mathcal{C}_F$ on an electron energy axis E_A. The map area corresponding to the selected final state has a shape of a rectangle with $E_B = E_{\gamma F} - E_A$ axis and $\pm\Delta$ breath (Fig. 1).

This is proportional to the following model quantity:

$$C_F(E_A;E_\gamma) = \int_{E_{\gamma F}-E_A-\Delta}^{E_{\gamma F}-E_A+\Delta} dE_B\, \mathcal{C}_F(E_A,E_B;E_\gamma). \quad (41)$$

Figures 6 and 7 compare simulated and experimental projections for Kr and Xe at several photon energies in the region of interest. The simulated trends agree very well with the experiment provided the spectrometer dead time is explicitly taken into account and the energy dependence of the photoionization cross section is accounted for. In accord with the expected strength of the effect, there is no experimental evidence of a significant interchannel exchange interference in the coincidence energy spectrum taken at 132.6 eV (89 eV) photon energy for Kr (Xe). On the other hand, the most prominent change (increase) of the coincidence yield due to intrachannel exchange effect is expected to occur exactly in the center of the dead-time area, not accessible for a direct verification (see below).

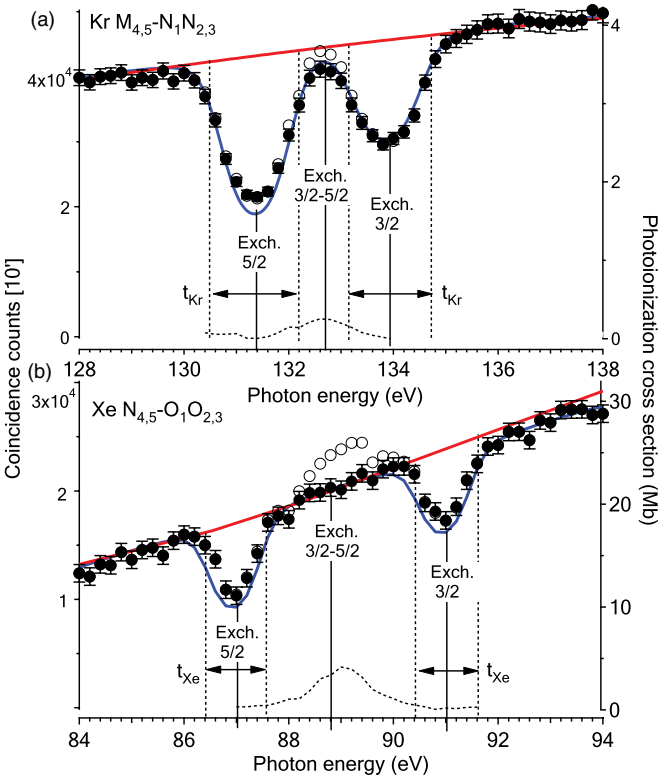

FIG. 8. (Color online) Black circles represent measured photon energy dependence of the total coincidence yield for the selected ^1P final state with false coincidence signal of 5/2 and 3/2 photoelectron pair removed (false coincidences: dotted line; empty circles: data before removal of false coincidences): (a) Kr, (b) Xe. Blue (gray) curve denotes calculated angle and energy integrated cross section with nonzero detector dead time. Red (light gray) line denotes calculated photoionization cross section according to Eq. (24). Vertical lines denote photon energies at which the interference effects are expected to be the most prominent and the dashed lines denote energy intervals where the detection of coincidence events is prevented by 6-ns detector dead time.

Figure 8 presents an integral of coincidence counts for the selected final state of Kr and Xe as a function of the photon energy. The predominant "spectral" feature is signal loss due the detector dead time at two critical photon energies fulfilling the condition for intra-channel exchange interference. No such instrumental effect is expected for the signal between the two dips, where the inter-channel interference is switched on, because there the photoelectron and Auger electron energies are different. There is, however, a small contribution of false coincidences of 5/2 and 3/2 photoelectrons. When this spurious signal is removed, a complete agreement with the calculated smooth photoabsorption cross-section behavior is obtained. This is consistent with expectations—the exchange interference effect is smoothed out in the photon energy spectrum.

A. Single-hit events and coincidence transfer

Unlike other techniques that map energy or angular dependence of electron yield on the MCP plane (COLTRIMS [55]), the position dependent detection of two electrons is not crucial for MB-TOF operation since two electrons emitted at different angles and with similar energy are expected to arrive at more or less the same place on the MCP detector. Although the nonzero dead time prevents detection of two electrons with equal energies, one can still extract information about interchannel exchange interference from the collection of single-hit events. A part of emitted photoelectron-Auger pairs is recorded as single-hit events because the electron detection efficiency is not perfect ($\eta < 1$), i.e., one electron of the pair does not trigger the MCP detector. On the other hand, when both electrons trigger the MCP detector within a small time interval, the nonzero detector dead time causes a perfect transfer of double-hit to single-hit events. If the frequency of single-hit events is traced as a function of photon energy, the transferred double-hit signal can be recovered. As shown below, a deviation of the single-hit signal at critical photon energies from the signal trend expected by extrapolation points to an "anomalous" rate of production of coincidence pairs—the intrachannel exchange interference. A similar approach was used recently for the detection of two-site ($K^{-1}K^{-1}$) events in a molecule that involves emission of four electrons [31]. As the Auger electrons of the equivalent atomic sites have practically the same energy, the evidence of these events was found in the three-electron coincidence spectrum. In Fig. 9(a), the number of collected single-hit events is plotted against the electron energy for photon impact energy of 140 eV in Kr. Except at critical photon energies, one may clearly recognize the pairs of photoelectron and Auger peaks related to the selected $(4s4p)^{-1}\,{}^1P$ final state. An electron emitted with about 38 eV energy, either photoelectron or Auger electron, is detected with an efficiency η determined by the collection solid angle and by the probability that the electron actually triggers the MCP detector. When at most one photoelectron-Auger pair is emitted per light pulse, the probability to detect both electrons from the same ionization event is η^2, and the probability to detect only the Auger electron is $\eta(1-\eta)$. As the pulse light intensity is relatively low, the experimental parameter η can be estimated with a few percent accuracy from the number of detected coincidence events and the number of Auger electrons detected by single-hit events, provided that the electron energies of the pair differ sufficiently to avoid the dead-time effect.

Further on we concentrate on a sequence of single-hit Kr spectra and define 0.4-eV wide energy windows centered at four relevant electron peaks [Fig. 9(a)]. The two photoelectron windows move along with the photon impact energy using exactly the same energy step, and the two Auger electron windows are at fixed energy positions. The number of events collected in both Auger windows and in both photoelectron windows is plotted against the incident photon energy in Figs. 9(b) and 9(c), respectively. In all windows, a gradually increasing "background" signal is observed, due to increase of the $3d$ photoionization cross section with the photon energy. Near the critical photon energies, where the windows overlap, signal changes are observed. In the absence of any interference and dead-time effects it is expected that the number of single-hit events for fully overlapped window(s) is given by the sum of single-hit events detected in the separated windows. Such an automatic increase can thus be estimated by interpolation of the window signals from the nonoverlapping

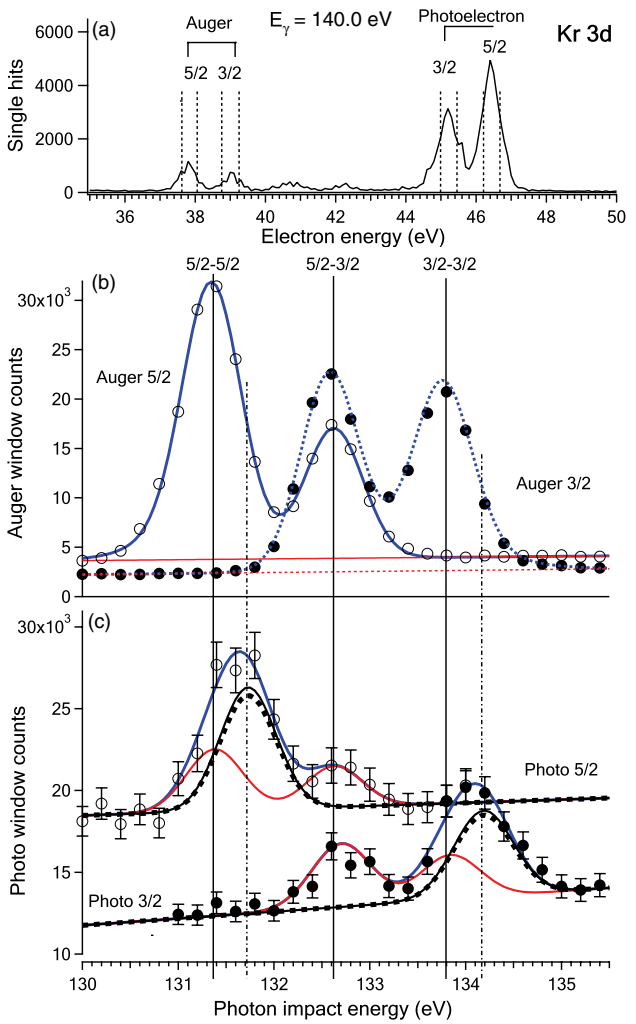

FIG. 9. (Color online) (a) A spectrum of single-hit events recorded in 10 min at 140.0-eV photon impact energy. Marked are the four energy windows centered on Kr 3*d* photoelectron lines and on Auger lines with the $(4s4p)^{-1}\,{}^1P$ final state. (b) Counts collected in both (fixed) Auger energy windows as a function of photon impact energy. Black (blue) solid line fits the 5/2 Auger signal and black (blue) dashed line fits the 3/2 Auger signal. The flat signal background is also shown in gray (red). (c) Counts collected in both (movable) photoelectron windows with respect to the photon impact energy. Gray (blue) line is an overall fit of data composed of two contributions: an overlap single-hit contribution (light gray, red line) and the energy shifted contribution (black line) of transferred double-hit events due to the nonzero detector dead time. The dashed black line is the double-hit transfer expected in the case of no intrachannel exchange interference. Solid vertical lines denote the critical photon energies and dot-dashed vertical lines denote maxima of the transferred counts.

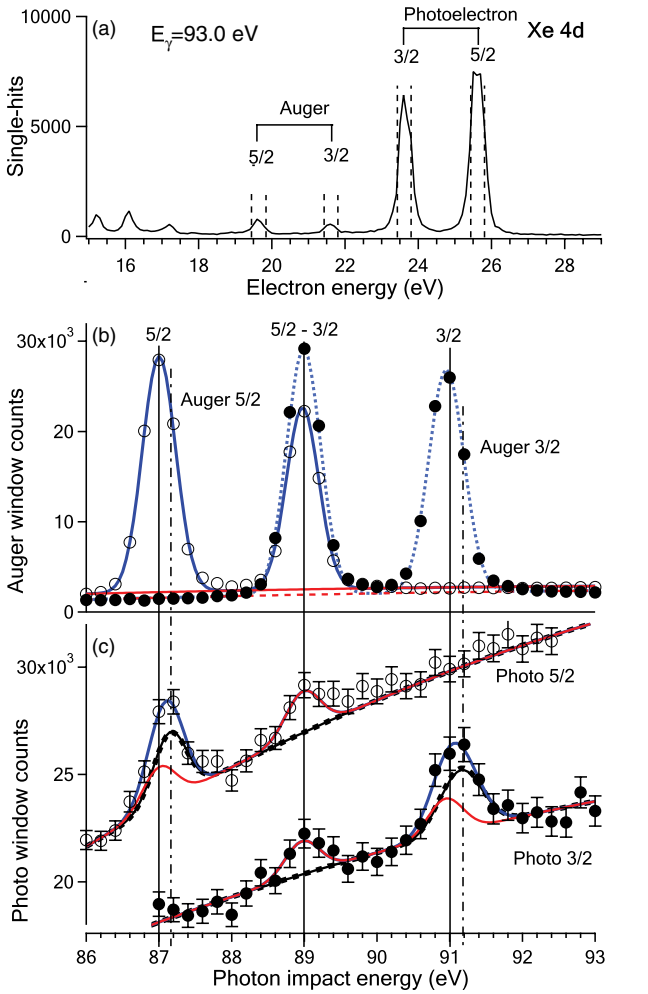

FIG. 10. (Color online) (a) Single-hit spectrum of Xe acquired in 10 min at 93-eV photon impact energy. (Movable) photoelectron and (fixed) Auger energy windows are denoted by vertical dashed lines. (b) Single-hit counts in the Auger energy window as a function of photon impact energy [5/2 channel: solid black (blue) line; 3/2 channel: dotted black (blue) line]. The single-hit counts at critical photon energies are obtained by interpolation of the flat background (red). (c) Single-hit counts in the photoelectron window as a function of photon impact energy. The light gray (red) line denotes an automatic increase of counts due to the overlap of lines in the single-hit spectrum. The black dotted line denotes an expected increase of transferred coincidence events caused by the detector dead time with no interchannel exchange interference effect. The gray (blue) line fits the actually observed increase with transferred counts contribution given by the black line. Solid vertical lines denote the critical photon energies and dot-dashed vertical lines denote maxima of the transferred counts.

energy region in Fig. 9(b). The photoelectron window signal is proportional to $\sigma^a(E_\gamma)\eta(1-\eta)$ and the Auger window signal is proportional to $\sigma^a(E_\gamma)\mathcal{B}^a\eta(1-\eta)$. In addition, there is a $\sigma^a(E_\gamma)\mathcal{B}^a\eta^2$ contribution to the single-hit signal at the critical photon energies, due to the double-hit events that appear as single-hit events because of the nonzero detector dead time. Assuming no interference, the expected photoelectron window signal jump at critical photon energy is

$$\sigma^a\mathcal{B}^a\eta(1-\eta)\left[1+\frac{\eta}{1-\eta}\right],$$

where the first term is due to an overlap single-hit contribution and the second term is due to the double-hit transfer. A detailed simulation of the coincidence transfer shows that for 20% constructive Kr 3*d* intra-channel exchange interference

about 4% increase of the transferred counts is expected when compared to the no-interference case. Such a loss of the signal contrast occurs because the available experimental resolution of 0.5 eV significantly surpasses the natural linewidth of the Kr $3d$ hole (0.1 eV). Setting the MB-TOF efficiency η to 0.65 in the relevant electron energy region, the no-interference transfer amounts to $\eta/(1-\eta) \approx 1.86$ times the (automatic) increase of the photoelectron signal due to the overlap with the corresponding Auger line. The fitting of the 5/2-photoelectron window signal results in a factor of 1.98 and the fitting of the 3/2-photoelectron window gives a factor of 1.95 [Fig. 9(c)]. Although such a discrepancy is hardly statistically significant, it points in the direction of a weak constructive intrachannel exchange interference in the angle-integrated cross section.

There is no transfer of double-hit events in case of the interchannel exchange interference since the photoelectron and the corresponding Auger electron have different energies. The signal in the photoelectron energy window is proportional $\sigma^a \eta(1-\eta)$, and when an energy overlap with the corresponding Auger energy window occurs, a signal increase of $\sigma^b \mathcal{B}^b \eta(1-\eta)$ is expected. As evident from Fig. 9(c), at 132.6-eV photon energy, the observed increase in the photoelectron yield is consistent with these expectations.

It is interesting to note that the transfer contribution to the photoelectron energy window reaches maximum at 0.35-eV higher photon energy with respect to the photon energy at which the photoelectron and the corresponding Auger window actually overlap. This shift is a consequence of the fact that it is always the arrival of the faster electron in a pair that gets transferred to single-hit events because of the dead-time effect. The shift of the maximum number of counts in the Auger window is expected to occur in the opposite direction. However, since the transferred counts represent a minor contribution with respect to the overlap contribution, the energy shift of the Auger signal is practically absent.

The shift is more prominent in Kr than in Xe because of the larger width of the dead-time zone in the energy space for Kr. For Xe $4d$ the result of a similar analysis is shown in Fig. 10. Taking the experimental $\eta \approx 0.63$ that applies at about 20 eV electron energy [Fig. 10(a)], the expected transfer contribution to the photoelectron window comes out as 1.74 times the extrapolated overlap single-hit contribution. The ratio that best describes the experimental data in Fig. 10(c) is 1.76 and 1.69 for the 5/2 and 3/2 photoelectron channel, respectively. There is no statistically significant discrepancy between the expected and the observed increase for the Xe case: 6% constructive interference contrast reduces down to 2% when the effect of experimental energy resolution is considered.

V. CONCLUSIONS

We have studied intra- and interchannel exchange interference in photoinduced Kr($N_{4,5}$–$O_1 O_{2,3}$) and Xe ($M_{4,5}$–$N_1 N_{2,3}$) Auger transitions. A decomposition of the $(\gamma,2e)$ cross section into a set of scalar invariants allows a straightforward comparison of the model results with the outcome of the previous noncoincidence and angular dependent $(\gamma,2e)$ studies. The concept remains useful when PCI is included in the model, since TDCS can be accessed either by factorization, or by the construction of a new set of weights combining the non-PCI weights with energy-dependent angular weights of the PCI factor. The analysis of the doubly differential cross section showed that PCI "contaminates" angular distribution by higher-order contributions to an extent that depends on the energy detuning. For the two studied cases, we estimate that PCI effects in the angle-integrated cross sections are smaller than the exchange interference effects.

The model was also applied to interpret fully angle-integrated (coincidence) spectra, measured by the magnetic bottle spectrometer for a sequence of photon energies. The interchannel interference effects in angle-integrated spectra are weak for the two investigated cases. They are estimated to be of the order of -1.0% (destructive) for the Xe case and $+0.5\%$ (constructive) for the Kr case when only the natural linewidth broadening is assumed. This is below the present experimental detection limit and indeed, no effects are visible in coincidence energy spectra measured at the corresponding critical photon energy. The intrachannel exchange interference effects that occur at equal electron energy sharing are expected to be larger and could not be directly assessed by the coincidence detection of electron pairs because of the nonzero dead time of the detector. Nevertheless, the analysis of the acquired single-hit energy spectra shows that the predicted constructive intrachannel exchange interference effects (+20% for Kr and +6% for Xe) agree with the acquired data when the experimental energy resolution is taken into account.

ACKNOWLEDGMENTS

This work was supported by the Research Programme P1-0112 of the Slovenian Research Agency. The experiments were performed at Soleil synchrotron (France) at the PLEIADES beamline, with the approval of the Soleil Peer Review Committee, under Project No. 20100278, and at Elettra synchrotron (Italy) at the GasPhase Photoemission beamline under Project No. 20120091. We are grateful to C. Nicolas and E. Robert for help during the measurements and to Soleil staff for stable operation of the storage ring during the experiments. Work was partially supported by the MAE Italy-Slovenia Joint project of particular relevance, "Dynamics at nanoscale."

[1] *Complete Scattering Experiments*, edited by U. Becker and A. Crowe, Physics of Atoms and Molecules (Kluwer Academic/Plenum Publishers, New York, 2001).

[2] U. Heinzmann, J. Phys. B **13**, 4353 (1980).

[3] J. Jimenéz-Mier, C. D. Caldwell, and D. L. Ederer, Phys. Rev. Lett. **57**, 2260 (1986).

[4] A. Hausmann, B. Kämmerling, H. Kossmann, and V. Schmidt, Phys. Rev. Lett. **61**, 2669 (1988).

[5] H.-J. Beyer, J. B. West, K. J. Ross, K. Ueda, N. M. Kabachnik, H. Hamdy, and H. Kleinpoppen, J. Phys. B **28**, L47 (1995).
[6] B. Kämmerling and V. Schmidt, Phys. Rev. Lett. **67**, 1848 (1991).
[7] J. B. West, K. J. Ross, K. Ueda, and H. J. Beyer, J. Phys. B **31**, L647 (1998).
[8] K. Ueda, Y. Shimizu, H. Chiba, Y. Sato, M. Kitajima, H. Tanaka, and N. M. Kabachnik, Phys. Rev. Lett. **83**, 5463 (1999).
[9] P. Bolognesi, A. De Fanis, M. Coreno, and L. Avaldi, Phys. Rev. A **70**, 022701 (2004).
[10] P. Bolognesi *et al.*, J. Phys. B **41**, 051003 (2008).
[11] M. Eminyan, K. B. MacAdam, J. Slevin, and H. Kleinpoppen, Phys. Rev. Lett. **31**, 576 (1973).
[12] N. Andersen, K. Bartschat, J. T. Broad, G. F. Hanne, and M. Uhrig, Phys. Rev. Lett. **76**, 208 (1996).
[13] Y. Morioka, T. Aoto, and H. Yoshii, Phys. Rev. A **64**, 053409 (2001).
[14] M. Alagia *et al.*, Phys. Rev. Lett. **102**, 153001 (2009).
[15] Y. Hikosaka, Y. Velkov, E. Shigemasa, T. Kaneyasu, Y. Tamenori, J. Liu, and F. Gelmukhanov, Phys. Rev. Lett. **101**, 073001 (2008).
[16] J.-E. Rubensson *et al.*, Chem. Phys. Lett. **257**, 447 (1996).
[17] K-H. Schartner *et al.*, J. Phys. B **40**, 1443 (2007).
[18] M. Kavčič, M. Žitnik, K. Bučar, A. Mihelič, S. Carniato, L. Journel, R. Guillemin, and M. Simon, Phys. Rev. Lett. **105**, 113004 (2010).
[19] J. P. Van den Brink, G. Nienhuis, J. van Eck, and H. G. M. Heideman, 1989, J. Phys. B **22**, 3501 (1989).
[20] L. Végh and J. H. Macek, Phys. Rev. A **50**, 4031 (1994).
[21] S. J. Schaphorst, A. Jean, O. Schwartzkopf, P. Lablanquie, L. Andrić, J. Mazeau, and V. Schmidt, J. Phys. B **29**, 1901 (1996).
[22] S. Rioual, B. Rouvellou, L. Avaldi, G. Battera, R. Camilloni, G. Stefani, and G. Turri, Phys. Rev. A **61**, 044702 (2000).
[23] O. Schwartzkopf and V. Schmidt, J. Phys. B **29**, 3023 (1996).
[24] J. Viefhaus, G. Snell, R. Hentges, M. Wiedenhöft, F. Heiser, O. Geßner, and U. Becker, Phys. Rev. Lett. **80**, 1618 (1998).
[25] P. Selles, J. Mazeau, P. Lablanquie, L. Malegat, and A. Huetz, J. Phys. B **31**, L353 (1998).
[26] L. Végh, Phys. Rev. A **50**, 4036 (1994).
[27] J. A. de Gouw, J. van Eck, A. C. Peters, J. van der Weg, and H. G. M. Heideman, Phys. Rev. Lett. **71**, 2875 (1993).
[28] J. A. de Gouw, J. van Eck, A. Q. Wollrabe, J. van der Weg, and H. G. M. Heideman, Phys. Rev. A **50**, 4013 (1994).
[29] S. Rioual, B. Rouvellou, A. Huetz, and L. Avaldi, Phys. Rev. Lett. **91**, 173001 (2003).
[30] J. H. D. Eland, O. Vieuxmaire, T. Kinugawa, P. Lablanquie, R. I. Hall, and F. Penent, Phys. Rev. Lett. **90**, 053003 (2003).
[31] P. Lablanquie *et al.*, Phys. Rev. Lett. **107**, 193004 (2011).
[32] H. Klar and M. Fehr, Z. Phys. D **23**, 295 (1992).
[33] http://www.synchrotron-soleil.fr/Recherche/LignesLumiere/PLEIADES
[34] J. Palaudoux, P. Lablanquie, L. Andric, K. Ito, E. Shigemasa, J. H. D. Eland, V. Jonauskas, S. Kučas, R. Karazija, and F. Penent, Phys. Rev. A **82**, 043419 (2010).
[35] K. C. Prince *et al.*, J. Synchrotron Radiat. **5**, 565 (1998).
[36] P. Bolognesi *et al.*, J. Electron Spectrosc. Relat. Phenom. **141**, 105 (2004).
[37] D. J. Kennedy and S. T. Mason, Phys. Rev. A **5**, 227 (1972).
[38] O. Zatsarinny, Comput. Phys. Commun. **98**, 235 (1996).
[39] A. F. Starace, in *Atomic, Molecular, and Optical Physics Handbook*, edited by G. W. F. Drake (AIP, Woodbury, NY, 1996), Chap. 24.
[40] K. G. Dyall, I. P. Grant, C. T. Johnson, F. A. Parpia, and E. P. Plummer, Comput. Phys. Commun. **55**, 425 (1989).
[41] D. W. Lindle, P. A.Heimann, T. A. Ferrett, P. H. Kobrin, C. M. Truesdale, U. Becker, H. G. Kerkhoff, and D. A. Shirley, Phys. Rev. A **33**, 319 (1986).
[42] B. Kammerling, B. Krassig, 0. Schwarzkopf, J. P. Ribeiro and V. Schmidt, J. Phys. B: At. Mol. Opt. Phys. **25**, L5 (1992).
[43] N. M. Kabachnik and I. P. Sazhina, J. Phys. B: At. Mol. Opt. Phys. **21**, 267 (1988).
[44] J. Tulkki, N. M. Kabachnik, and H. Aksela, Phys. Rev. A **48**, 1277 (1993).
[45] D. W. Lindle, T. A. Ferrett, P. A. Heimann, and D. A. Shirley, Phys. Rev. A **37**, 3808 (1988).
[46] E. G. Berezhko, N. M. Kabachnik, and V. S. Rostovsky, J. Phys. B.: At. Mol. Phys. **11**, 1749 (1978).
[47] G. Snell, E. Kukk, B. Langer, and N. Berrah, Phys. Rev. A **61**, 042709 (2000).
[48] S. Southworth, U. Becker, C. M. Truesdale, P. H. Kobrin, D. W. Lindle, S. Owaki, and D. A. Shirley, Phys. Rev. A **28**, 261 (1983).
[49] S. P. Shannon, K. Codling, and J. B. West, J. Phys. B: At. Mol. Phys. **10**, 825 (1977).
[50] U. Becker, D. Szostak, H. G. Kerkhoff, M. Kupsch, B. Langer, and R. Wehlitz, A. Yagishita, and T. Hayaishi, Phys. Rev. A **39**, 3902 (1989).
[51] L. 0. Werme, T. Bergmark and K. Siegbahn, Phys. Scr. **6**, 141 (1972).
[52] A. Kivimäki, L. Pfeiffer, H. Aksela, E. Nõmmiste, and S. Aksela, J. Electron Spectrosc. Relat. Phenom. **101-103**, 43 (1999).
[53] S. A. Sheinerman and V. Schmidt, J. Phys. B: At. Mol. Opt. Phys. **30**, 1677 (1997).
[54] B. Rouvellou, S. Rioual, L. Avaldi, R. Camilloni, G. Stefani, and G. Turri, Phys. Rev. A **67**, 012706 (2003).
[55] J. Ullrich *et al.*, Rep. Prog. Phys. **66**, 1463 (2003).